Microsyst Technol (2011) 17:483–493
DOI: 10.1007/s00542-011-1258-2

TECHNICAL PAPER

Modeling Analysis of a Triaxial Microaccelerometer with Piezoelectric Thin-Film Sensing Using Energy Method

Jyh-Cheng Yu · Chungda Lee · Weinan Kuo
Chiaokai Chang

The original publication is available at www.springerlink.com, http://dx.doi.org/10.1007/s00542-011-1258-2

Received: 26 June 2010 / Accepted: 4 February 2011 / Published online: 23 February 2011

Abstract This study applies energy method to derive the system modeling of a triaxial micro-accelerometer that consists of a quadri-beam suspension, a seismic mass, and displacement transducers using piezoelectric thin films. Two suspension beams support both ends of the seismic mass, which is fabricated by anisotropic etching of silicon. An out-of-plane acceleration will result in a symmetric bend, and in-plane accelerations will produce asymmetric bend and torsion of the suspension beams. Two piezoelectric thin-film transducers are arranged at both ends of each suspension beam. Eight transducers in total are interconnected such that triaxial accelerations can be measured selectively. The structure stiffness of the suspension beams considers both the silicon beams and piezoelectric films by the use of the laminated beam theory. Therefore, the analytical model is applicable to the accelerometers with thick piezoelectric films. The model is based on the anisotropic material properties of Silicon and PZT and Euler's beam equation with the assumptions that smaller strains and stresses are negligible. The analytical results of the resonant frequencies and sensor sensitivities to triaxial accelerations are presented and confirmed by finite element analysis.

J.-C. Yu* · W. Kuo
National Kaohsiung First University of Science and Technology,
2, Juoyue Rd., Nantz District, Kaohsiung 811, Taiwan, ROC.
* Corresponding Author: jcyu@nkfust.edu.tw

C. Lee · C. Chang
I-Shou University, No. 1, Sec. 1, Syuecheng Rd., Dashu,
Kaohsiung 840, Taiwan, ROC

1. Introduction

For decades, miniaturized accelerometers have been widely applied to designs of automobile such as automatic braking systems, suspension control, airbags and navigation systems to improve driving safety, comfort, performance and controllability. Applications in interactive entertainment and communication electronics also show increasing potential markets. Typical microaccelerometers are based on piezoresistive (Lowrie et al. 2009; Takao et al. 2001) and capacitive (Lemkin et al. 1997; Chae et al. 2005) principles. Piezoelectric accelerometers have the advantages of excellent dynamic performance, high linearity, simple structure and easy integration with existing measuring electronic systems. Surface micromachined piezoelectric accelerometers are fabricated using standard VLSI processing techniques (DeVoe and Pisano 2001). However, bulk micromachining-based piezoelectric accelerometers have a lower detection level that is suitable for precision measurement. Recent research of piezoelectric sensors shows increased interest in preparing piezoelectric thin films, such as ZnO, AlN, and PZT on structure substrates instead of using bulk piezoelectric crystal because of a lower cost.

Typical configurations of a bulk micromachined accelerometer include a seismic mass supported by single or multiple suspension beams (Yu and Lan 2001). Thin film piezoelectric transducers are arranged on the suspension beams to convert induced stresses into output charge. Single crystal silicon is an anisotropic material. Depending on the fabrication processes of silicon-based accelerometers, such as chemical wet etching and deep reactive ion etching (DRIE), the crystal orientation of supported beam will be selected. The suspension beams

of the accelerometers using DRIE-based process can be patterned along any crystalline direction of silicon, but often aligned with [100] directions. On the other hand, wet etching-based process has a great cost advantage at the expense of dimensional constraints due to angled sidewalls and compensation pattern for convex corners. Therefore, the mass is shaped like a truncated pyramid, and the suspension beams have to align with [110] directions. Corresponding stiffness matrices of silicon should be adopted in the following derivation of theoretical model and finite element simulations.

If the mass is relatively small and the thickness of suspension beams is relatively thin compared with those of the seismic mass, the mechanical structure can be simplified into a spring-mass-damping system. Van Kampen and Woffenbuttel (1998) presented a detailed mechanical modeling for bulked-micromachined silicon accelerometers. The design and characterization of a single axis piezoelectric accelerometer has been well explored (Wang et al. 2003; Wang et al. 2004; Yu and Lan 2001). Their proposed theoretical models agree well with finite element analysis (FEA). A few attempts have so far been made at design and modeling of triaxial piezoelectric microaccelerometers. Two arrangements of suspension beams are reported: a cross type and a parallel type as shown in Fig. 1. Both configurations adopt a central seismic mass and four suspension beams with one beam at each lateral side of the mass for the cross type, and two parallel beams at both ends of the mass for the parallel type.

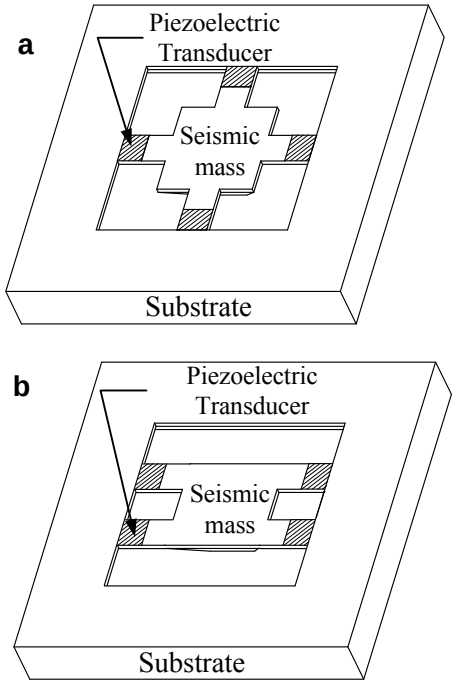

Fig. 1 Typical suspension configurations of piezoelectric triaxial microaccelerometers **a.** Cross beam design **b.** Parallel beam design

Hindrichsen et al. (2009) presented a mechanical model based on full anisotropic material tensors and Euler's beam equation for the PZT thick-film triaxial microaccelerometer of a cross beam configuration. Parametric design of the accelerometer was proposed to achieve equal sensitivity in all three directions. However, the cross-beam configuration and the short beam design cause an undesirable cross-axis sensitivity which degrades the measurement accuracy of the accelerometer. Kunz et al. (2001) presented a micromachined triaxial single-mass accelerometer of a cross beam configuration using PZT thin films and DRIE-based process of SOI wafers to demonstrate the design feasibility. Zou et al. (2008) reported a triaxial accelerometer of a similar configuration but built on symmetric bimorph beams using parylene and ZnO films to support a wet etched seismic mass.

Zhu et al. (2004) proposed a Lagrange's formulation for the dynamic model of a triaxial micro-accelerometer with piezoelectric thin-film sensing using the supported configuration of parallel beams. A laminated beam theory was applied to take into account both the substrate and PZT thin film in elastic properties of suspension beams. The comparison result of the sensitivities between analytical model and FEA show a difference around 10% for symmetrical and asymmetrical bending. The study claimed that the sensitivities of both directions of the in-plane acceleration are the same. However, the structure stiffness parallel to the supported beams and the structure stiffness perpendicular to the supported beams are different in Fig. 1b, and should be derived separately to obtain accurate sensitivity predictions.

This study will present a system modeling of a triaxial accelerometer including the mechanical and piezoelectric subsystems. The suspension configuration adopts parallel beams at both ends of a seismic mass using anisotropic etching of (100) silicon. The elastic property of the suspension beams considers both the silicon beams and the piezoelectric films by the use of the laminated beam theory. Energy method is applied to derive the suspension stiffness for three directions of accelerations. The interconnections among transducers are proposed to eliminate the cross-axis sensitivity. Analytical results of the resonant frequency and the charge sensitivity are compared with FEA results to verify the model accuracy.

2. Design of microaccelerometer

The proposed microaccelerometer consists of a seismic mass end supported by two pairs of parallel beams as shown in Fig. 2. A typical device is fabricated using a backside anisotropic wet etching of (100) SOI wafer for

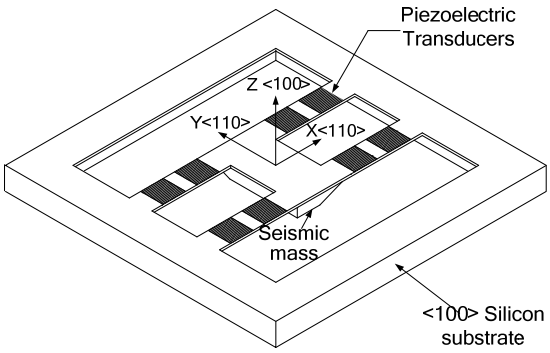

Fig. 2 Design of the accelerometer and the deployment of piezoelectric transducers

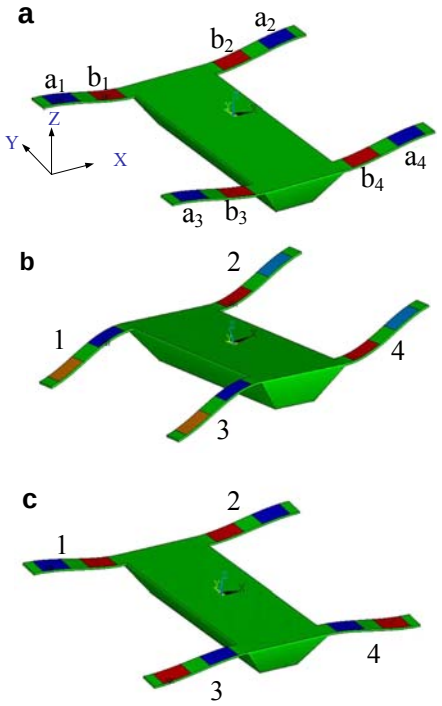

Fig. 3 Three basic vibration modes of the accelerometer due to triaxial accelerations **a.** Symmetric bend (*Z*-axis) **b.** Asymmetric bend (*X*-axis) **c.** Torsional (*Y*-axis)

a seismic mass and deep reactive ion etching of the front for suspension beams. Two transducers are patterned on each suspension. Each transducer consists of a lower electrode, a piezoelectric thin film and an upper electrode. The placements of the transducers are slightly away from the fixed and the seismic ends to avoid the stress nonlinearity due to the finite rigidity of the supported frame and the seismic mass. Also, the mid section of the beam is not suitable for transducer placement because of low stress.

The out-of-plane (*Z* axial) acceleration will introduce a symmetric vibration, and in-plane (*X* and *Y* axial) accelerations will produce asymmetric and torsional vibrations. The inertia force will cause bending and torsional stresses of the beams that produce output charge by the piezoelectric transducers. All the piezoelectric thin films are poled in the same direction along the thickness. Two transducers are patterned symmetrically on each beam. Transducers a_i are adjacent to the supported frame and transducers b_i are adjacent to the seismic mass. There are in total eight charge signals that are converted into eight open circuit voltages. For all three principal vibration modes, the transducers on the same beam are always of opposite phases as shown in Fig. 3. Therefore, the subtraction of two voltage outputs, $V(a_i\text{-}b_i)$, will increase transducer sensitivities. The electrodes on four beams are interconnected as in Table 1, such that the three axial accelerations can be selectively measured without cross effects. For instance, the *Z*-axial (vertical) acceleration will cause symmetrical bending of the supported beams as shown in Fig. 3a. All beams are subject to the same bending. On the other hand, *X*-axial accelerations cause asymmetric bending of the supported beams as shown in Fig. 3b. The bending stresses of the transducers on beams 2 and 4 are in opposite phases to those of the transducers on beams 1 and 3. Similarly, *Y*-axial accelerations cause the bending and torsion of the supported beams as shown in Fig. 3c. The bending stresses of the transducers on beams 1 and 2 are in opposite phases to those of the transducers on beams 3 and 4, while the torsional stresses of all the transducers are of the same phase. A piezoelectric transducer can be treated as a capacitance, and the generated charge can be converted into a voltage signal from a pertinent circuit design. Therefore, the voltages collected from the transducers a_1, a_2, a_3 and a_4 minus the voltages collected from the transducers b_1, b_2, b_3 and b_4 will be in proportional to vertical accelerations while the effects due to in-plane accelerations will be cancelled out. Similar situations apply when measuring the in-plane accelerations using the corresponding interconnection design shown in Table 1. This design not only increases transducer sensitivities, but also removes cross-axis effects.

3. Static system modeling

The system model of the accelerometer can be divided into a mechanical subsystem and a piezoelectric subsystem. The mechanical transfer function can be obtained according to Newton's second law for a

Table 1 Interconnection arrangement of the transducers for triaxial acceleration sensing

Symmetric	$V(a_1\text{-}b_1) + V(a_2\text{-}b_2) + V(a_3\text{-}b_3) + V(a_4\text{-}b_4)$
Asymmetric	$-V(a_1\text{-}b_1) + V(a_2\text{-}b_2) - V(a_3\text{-}b_3) + V(a_4\text{-}b_4)$
Torsional	$V(a_1\text{-}b_1) + V(a_2\text{-}b_2) - V(a_3\text{-}b_3) - V(a_4\text{-}b_4)$

simplified spring-mass-damper system. The performance of the mechanical subsystem is determined by the equivalent stiffness of the suspension and the seismic mass. The suspension stiffness is derived using energy method, and laminated beam theory is applied to obtain the equivalent bending rigidity of the supported beams. The piezoelectric transducers convert beam stresses into output charge.

3.1. Structure Modeling

The derivation of the structure model of the proposed accelerometer is based on the following assumptions:

1. the influence of electrodes on the beam stiffness is negligible;
2. the seismic mass and rim of the structure are rigid;
3. the deflections of substrate material and piezoelectric films of supported beams observe linear elasticity and Hooke's Law;
4. the piezoelectric material is anisotropic;
5. the supported beams are wide and flat, and thin beam theory (Euler-Bernoulli beam model) is applied; the stresses in the z-direction and the strains in the y-direction are negligible (van Kampen and Wolffenbuttel 1998) compared with others. Therefore,

$$\sigma_3 = \sigma_4 = \sigma_5 = 0$$
$$\varepsilon_2 = \varepsilon_4 = \varepsilon_5 = 0 \tag{1}$$

The corresponding mechanics coordinates shown in Fig. 3 for the Voigt notations are as follows:

$$\begin{pmatrix} \sigma_1 \\ \sigma_2 \\ \sigma_3 \\ \sigma_4 \\ \sigma_5 \\ \sigma_6 \end{pmatrix} = \begin{pmatrix} \sigma_{xx} \\ \sigma_{yy} \\ \sigma_{zz} \\ \tau_{yz} \\ \tau_{xz} \\ \tau_{xy} \end{pmatrix} \tag{2}$$

Thin beam theory can be applied when the ratio of the length to the thickness of the beam is larger than 10, and the beam is under small flexure deformation. Based on the assumptions, rotation of differential element is negligible in comparison with translation, and angular distortion caused by shear is relatively small compared to bending deformation. Therefore, the effects of the rotary inertia and shear deformation can be neglected. Since the piezoelectric thin film such as PZT is assumed as an anisotropic material, the constitutive equation can be simplified as follows:

$$\begin{pmatrix} \sigma_1 \\ \sigma_2 \\ \sigma_3 \\ \sigma_6 \end{pmatrix} = \begin{pmatrix} C_{p,11} & C_{p,12} & C_{p,13} & 0 \\ C_{p,21} & C_{p,22} & C_{p,23} & 0 \\ C_{p,31} & C_{p,32} & C_{p,33} & 0 \\ 0 & 0 & 0 & C_{p,66} \end{pmatrix} \begin{pmatrix} \varepsilon_1 \\ \varepsilon_2 \\ \varepsilon_3 \\ \varepsilon_6 \end{pmatrix} \tag{3}$$

Multiply out the expression for σ_3 and substitute the stress/strain assumptions in (1), we have

$$\varepsilon_3 = -\frac{C_{p,31}}{C_{p,33}}\varepsilon_1 \tag{4}$$

Similarly, with the aid of (4), stress σ_1 can be represented as follows:

$$\sigma_1 = \left(C_{p,11} - \frac{C_{p,13}C_{p,31}}{C_{p,33}} \right)\varepsilon_1 = E_P\varepsilon_1 \tag{5}$$

$$E_P = C_{p,11} - \frac{C_{p,13}C_{p,31}}{C_{p,33}} \tag{6}$$

where E_p is the effective modulus of elasticity for the piezoelectric film.

A typical fabrication process of the accelerometer consists of anisotropic wet etching of (100) silicon for the seismic mass and Inductively Coupled Plasma (ICP) etching for the supported beams. The geometry of the seismic mass is a truncated pyramid because of the crystal orientation of (100) silicon. The directions along the length and the width of the supported beams are in the [110] direction of silicon. Therefore, the stiffness matrix of silicon corresponding to the crystal axis coordinate system has to be transformed to the device coordinate system (Wortman and Evans 1965) as shown in Fig. 2.

Also, the cross section of the supported beams is assumed to be wide and flat, and under the plane stress condition. Therefore, the effective modulus of elasticity for the silicon beams can be derived similarly to the process for the PZT thin film as (7).

$$E_B = C_{S,11} - \frac{C_{S,13}C_{S,31}}{C_{S,33}} \tag{7}$$

where $C_{S,11}$, $C_{S,13}$, $C_{S,13}$ and $C_{S,33}$ are the stiffness coefficients of silicon beams.

Here we apply laminated beam theory to derive the equivalent bending rigidity (Gere and Timoshenko 1997). Fig. 4a is a schematic cross section of the laminated piezoelectric film / silicon beam. Y is the neutral axis of the section. E_P and E_B are the equivalent moduli of elasticity of the piezoelectric film and the substrate layer respectively. The laminated beam can be treated as an equivalent beam of the same material as substrate layer with the width of the piezoelectric layer adjusted according the elasticity ratio to the substrate material's as shown in Fig. 4b. The distance of the neutral axis to the interface can then be obtained as (8).

$$a = \frac{1}{2}\frac{E_B{t_b}^2 - E_P{t_p}^2}{E_B t_b + E_P t_P} \tag{8}$$

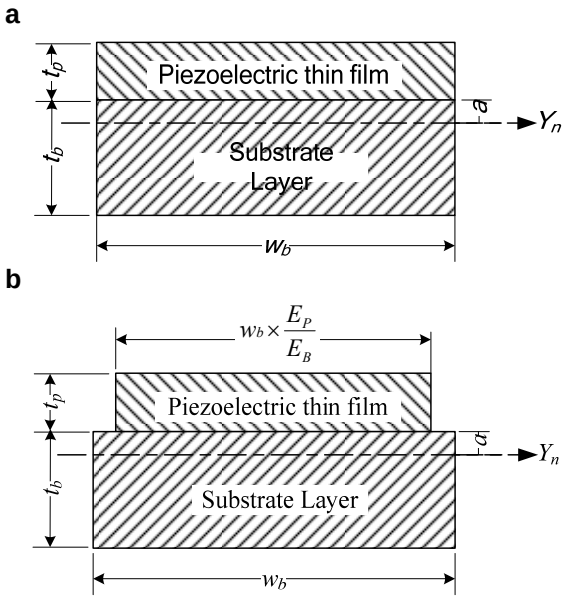

Fig. 4 Cross section of the piezoelectric film/Si beam **a.** Original composite beam **b.** Equivalent composite beam

By parallel axis theorem, the equivalent moment of inertia about *Y*-axis can be derived, and the equivalent bending rigidity of the composite beam is as follows:

$$(EI_Y)_{eq} = E_P w_b \left(\frac{t_P^{\,3}}{3} + t_P^2 a + t_P a^2 \right) + E_B w_b \left(\frac{t_b^{\,3}}{3} - t_b^2 a + t_b a^2 \right) \tag{9}$$

3.2. Symmetric Bend due to a Z-axial (Vertical) Acceleration

Fig. 5b shows the schematic free-body diagram of the accelerometer subject to a vertical acceleration. This study applies energy method - Castigliano's second theorem to derive structure stiffness. For a linear structure the partial derivative of the strain energy with respective to an applied load, such as inertial force F_i and bending moment M_i, is equal to the corresponding displacements δ_i and α_i.

$$\delta_i = \frac{\partial U}{\partial F_i} \tag{10}$$

$$\alpha_i = \frac{\partial U}{\partial M_i} \tag{11}$$

$$U = \int_0^{l_b} \frac{M(\xi)^2}{2EI} d\xi \tag{12}$$

where U is the strain energy, M represents the bending moment, and EI is the flexural rigidity of the supported beam. The bending moment equilibrium equation and the

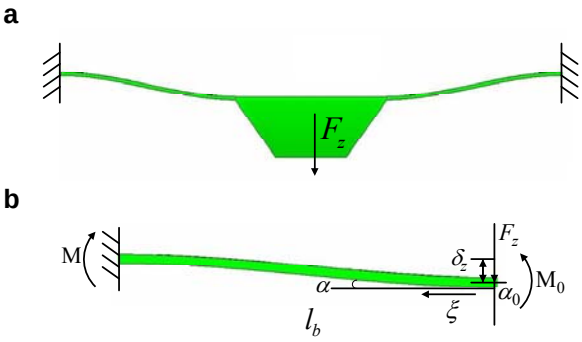

Fig. 5 Symmetric bending of the accelerometer **a.** Symmetric bending **b.** Free body diagram of suspension beam

boundary conditions for the free body diagram of Fig. 5b are as follows:

$$M(\xi) + F_z \xi - M_0 = 0 \tag{13}$$

$$\xi=0 \quad \delta_z(0)=\delta_z \quad \alpha(0)=0$$
$$\xi=l_b \quad \delta_z(l_b)=0 \quad \alpha(l_b)=0 \tag{14}$$

The structure can be simplified as a spring-mass system. The out-of-plane resonant frequency $f_{n,s}$ can be obtained as follows:

$$f_{n,s} = \frac{1}{2\pi}\sqrt{\frac{K_s}{m_{t,s}}} \tag{15}$$

$m_{t,s}$ is the equivalent mass of the system and K_s is the stiffness of the suspension for the symmetric vibration. The equivalent mass can be obtained as follows,

$$m_{t,s} = m + 4m_{eq,s} \tag{16}$$

where m is the seismic mass, and $m_{eq,s}$ is the effective mass of the supported beam in symmetric vibration. The seismic mass consists of a truncated long pyramid with the base angle θ of 54.74° due to the anisotropic wet etching such as KOH, a rectangle silicon top from the relief of suspension beams using ICP etching, and the piezoelectric film. Neglecting possible imperfections of the convex corner compensation for anisotropic wet etching of the (100) silicon wafer, a simple integration of the structure will give the seismic mass:

$$m = \rho \cdot \left[l_m w_m h_m - \frac{1}{\sqrt{2}} h_m^{\,2} (l_m + w_m) + \frac{2}{3} h_m^{\,3} \right] + \rho \cdot l_m w_m t_b + \rho_{pzt} l_m w_m t_p \tag{17}$$

where ρ is the density of silicon, ρ_{pzt} is the density of PZT, and l_m, w_m, h_m, t_b, and t_p are the dimensions of the seismic mass as shown in Fig. 6.

The stiffness for the symmetric vibration can be derived as follows (Yu and Lan 2001),

$$K_s = \frac{48(EI_Y)_{eq}}{l_b^3} \tag{18}$$

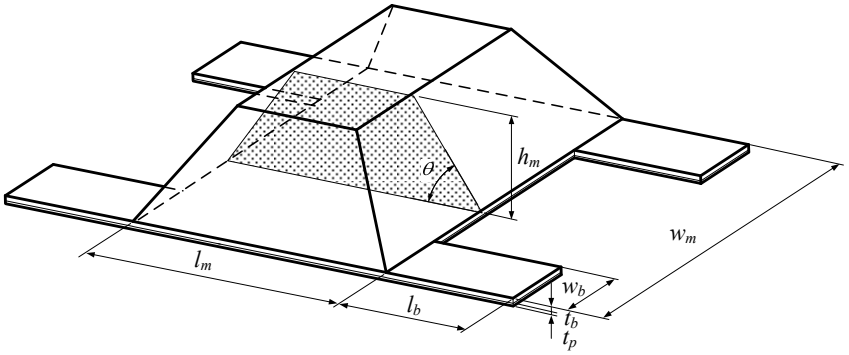

Fig. 6 Geometric parameters for the proposed accelerometer design

where $(EI_Y)_{eq}$ is the equivalent bending rigidity about Y axis, and l_b is the length of the suspension beam.

The effective mass of the supported beams, $m_{eq,s}$, can be derived by kinetic energy method (Thomson and Dahleh 1998). If the deflection is small, the differential equation of the deflection of beam is approximated according to Hooke's law. Solving the differential equation with the boundary conditions yields the deflection of the suspension beams. The kinetic energy of a suspension beam, T is treated as those of an effective lump mass, $m_{eq,s}$ with the displacement δ_z that is the deflection at the end of the beam.

$$T = \frac{1}{2} m_{eq,s} \dot{\delta}_z^2 \tag{19}$$

$$m_{eq,s} = c_{m,s}(m_b) \tag{20}$$

where $\dot{\delta}_z$ is the velocity at the end of the supported beam, m_b is the real mass of the laminated beam, and $c_{m,s}$ is the effective constant which is 13/35 for the symmetric vibration case.

From the free-body diagram of Fig. 5b, the bending moment along the supported beam for a given displacement δ_Z of the seismic mass can be represented as (21).

$$M(\xi) = \frac{6(EI_Y)_{eq}\delta_z}{l_b^{\,2}} - \frac{12(EI_Y)_{eq}\delta_z}{l_b^{\,3}}\xi \tag{21}$$

The bending stress across the piezoelectric thin film is linearly distributed according to the assumption of small flexural deformation. The total generated charge of the piezoelectric film due to the bending moment can be represented a function of the average bending stress σ_1 which can be derived as follows:

$$\sigma_1(\xi) = \frac{M(\xi)}{I_{eq}}\left(\frac{t_P}{2} + a\right)\cdot\left(\frac{E_P}{E_B}\right) \tag{22}$$

If the stresses other than σ_1 caused by bending of the piezoelectric film are negligible and no external electrical field is applied, the contribution from an infinitesimal portion of the piezoelectric material to the total charge is as follows:

$$D_3 = d_{31}\sigma_1(\xi) \tag{23}$$

where d_{31} is the transverse piezoelectric charge to stress ratio.

If the interconnection of the piezoelectric transducers is as Table 1 and the dimensions of the transducers are as Fig. 7, substituting (22) into the integration of (23) along a suspension beam yields the charge output of the piezoelectric films:

$$\begin{aligned} Q_{s,b} &= \int_{\frac{1}{10}l_b}^{\frac{4}{10}l_b} D_3 w_b d\xi - \int_{\frac{6}{10}l_b}^{\frac{9}{10}l_b} D_3 w_b d\xi \\ &= \frac{9\delta_Z w_b d_{31} E_P}{5l_b}\left(\frac{t_P}{2} + a\right) \end{aligned} \tag{24}$$

The displacement of the seismic mass can be obtained from Hook's law and (18) as follows:

$$\delta_Z = \frac{m_t a_Z l_b^{\,3}}{48(EI_Y)_{eq}} \tag{25}$$

All four beams produce the same output due to the symmetric vibration. Because of the arrangement of the transducers as Table 1, the sensor's open-circuit voltage sensitivity S_Z is as follows:

$$S_Z = \frac{V_Z}{a_Z} = \frac{4Q_{s,b}}{a_Z C_t} = \frac{m_t d_{31} E_P l_b t_P}{2(EI_Y)_{eq}\varepsilon_{33}}\left(\frac{t_P}{2} + a\right) \tag{26}$$

where C_t is the capacitance of the piezoelectric transducer, and ε_{33} is the dielectric permittivity of the piezoelectric film.

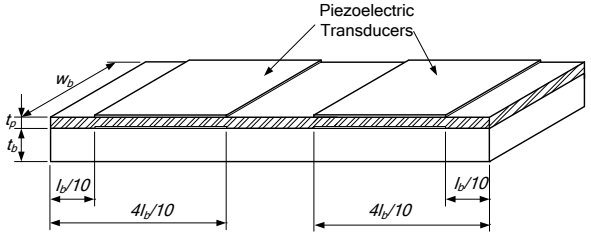

Fig. 7 Layout design of the piezoelectric transducers on a suspension beam

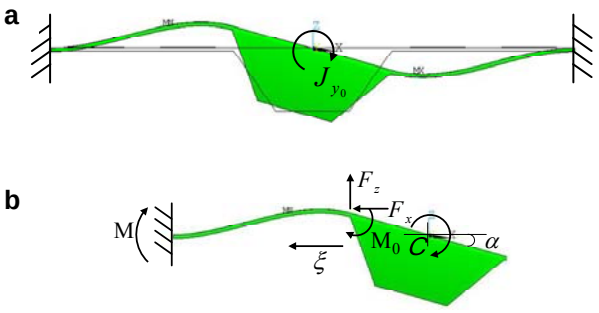

Fig. 8 Asymmetric bending of the accelerometer **a.** Asymmetric bending **b.** Free body diagram of the suspension beam

3.3. Asymmetric Bend due to an X-axial Acceleration

Fig. 8 is the schematic free-body diagram of the accelerometer subject to an *X*-axial acceleration. The acceleration causes a net force $F_x=ma_x$ on the center of the seismic mass, which results in the rotation of mass around center point *C* which is at the neutral axis of the supported beam as shown in Fig. 9. The rotation of the seismic mass introduces a displacement and a bending moment at the ends of the supported beams. The seismic mass can be treated as a lump mass supported by two parallel springs. The spring constant due to the end displacement of the beam is $K_{a,4\delta}$ as (27), and the other due to the bending of the beam to conform the rotation angle of the mass is $K_{a,\alpha}$ as (28).

$$K_{a,4\delta} = \frac{48(EI_Y)_{eq}(l_m+l_b)}{l_m \cdot l_b^{\,3}} \tag{27}$$

$$K_{a,\alpha} = \frac{4(EI_Y)_{eq}(3l_m+4l_b)}{l_b^{\,2}} \tag{28}$$

Because the distance between the end of the beam and the rotating center *C* is $l_m/2$, the effective torsional stiffness, $K_{a,\delta}$ due to the end displacement of the beam with respect to the rotating center is as (29).

$$K_{a,\delta} = K_{a,4\delta} \cdot \left(\frac{l_m}{2}\right)^2 \tag{29}$$

Therefore, the equivalent torsional stiffness of the asymmetric vibration mode can be represented as follows:

$$K_{a,s} = K_{a,\alpha} + K_{a,\delta} = \frac{4(EI_Y)_{eq}(3l_m+4l_b)}{l_b^{\,2}} + \frac{12(EI_Y)_{eq}l_m(l_m+l_b)}{l_b^{\,3}} \tag{30}$$

The resonant frequency of this rotational system is

$$f_{n,as} = \frac{1}{2\pi}\sqrt{\frac{K_{a,s}}{J_{Yeq}}} \tag{31}$$

J_{Yeq} is the equivalent rotational moment of inertia of the accelerometer about *Y*-axis,

$$J_{Yeq} = J_{my} + 4(J_{by})_{eq} \tag{32}$$

where J_{my} is the rotational moment of inertia of the seismic mass about the *Y*-axis, and $(J_{by})_{eq}$ is the effective rotational moment of inertia of a supported beam about *Y*-axis. The derivation of J_{my} is straight forward. The effective rotational moment of inertia of the supported beams can be determined using kinetic energy method (Thomson and Dahleh 1998).

$$(J_{by})_{eq} = \frac{(l_b^2 - 5l_b l_m + 8l_m^2)\cdot m_b}{105} \tag{33}$$

Following a similar integration as (24), the generated charge of a single beam is as follows:

$$Q_{a,b} = \frac{9\alpha w_b d_{31} E_P (l_m+l_b)}{10 l_b} \cdot \left(\frac{t_P}{2}+a\right) \tag{34}$$

where α is the rotation angle of the seismic mass, which can be obtained by dividing the torque due to the inertial force of the accelerations in *X*-axis by the equivalent torsional stiffness of the asymmetric vibration mode (30) as follows:

$$\alpha = \frac{m_{total,a}\cdot a_x \cdot Z_{c,a}\cdot l_b^{\,3}}{4(EI_Y)_{eq}l_b(3l_m+4l_b)+12(EI)_{eq}l_m(l_m+l_b)} \tag{35}$$

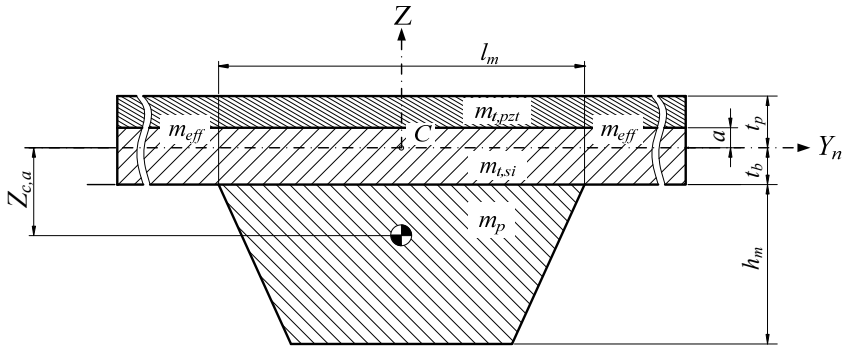

Fig. 9 Location of the equivalent system mass center for the asymmetric vibration mode

where $m_{total,a}$ is the equilivant total mass for the asymmetric vibrating mode, a_x is the applied acceleration in X-axis, and $Z_{c,a}$ is the distance between the equivalent system mass center for the asymmetric vibration mode and the neural axis as shown in Fig. 9.

$$m_{total,a} = m + 4 \cdot m_{eq,a} \tag{36}$$

$m_{eq,a}$ is the effective mass of the supported beam in the asymmetric vibration that can be determined by (37).

$$m_{eq,a} = \frac{(J_{by})_{eq}}{r_a^2} \tag{37}$$

where $r_a=l_m/2$ is the rotational radius about center C.

Because of the design symmetry, the voltages collected from each beam, $V(a_i\text{-}b_i)$, for the asymmetric vibration mode will be of the same magnitude but different phases. Using the interconnection arrangement of the transducers as Table 1, the sensor's open-circuit voltage sensitivity S_x for X-axial accelerations is as follows:

$$S_x = \frac{V_x}{a_x} = \frac{4Q_{a,b}}{a_x C_t} = \frac{12\alpha d_{31} E_p t_p (l_m + l_b)}{l_b^2 \varepsilon_{33} a_x}\left(\frac{t_p}{2} + a\right) \tag{38}$$

3.4. Torsion due to a Y-axial Acceleration

Fig. 10 is the schematic free-body diagram of the accelerometer subject to a Y-axial acceleration. The acceleration causes a net force $F_y=ma_y$ on the center of the seismic mass, which results in the rotation of mass about X-axis. The rotation of the seismic mass causes a displacement of different directions for the two supported beams at one end of the mass. Follow a similar derivation procedure of the asymmetric vibration; the equivalent torsional stiffness can be derived as follows:

$$K_{ts} = \frac{48(EI_Y)_{eq}}{l_b^3} \cdot \left(\frac{w_m - w_b}{2}\right)^2 + 4 \cdot \frac{c_2 w_b t_b^3 G}{l_b} \tag{39}$$

where G = 79.6 (GPa) is the shear modulus of silicon (Wortman and Evans 1965), and c2 is the torsional constant that is 0.333 for a wide and thin, $\left(\frac{w_b}{t_b + t_p} \geq 10\right)$, rectangular cross section (Timoshenko and Goodier 1970).

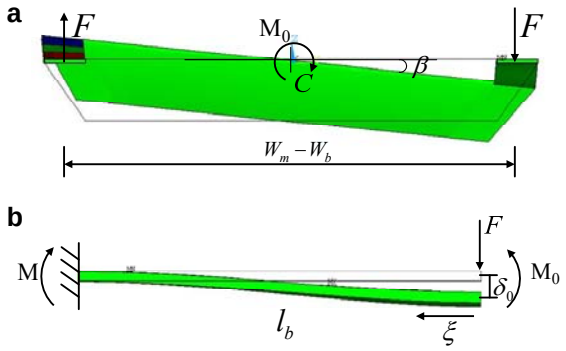

Fig. 10 Torsional bending of the accelerometer **a.** Torsional bending **b.** Free body diagram of suspension beam

The resonant frequency of this rotational system for the torsional vibration mode is

$$f_{n,t} = \frac{1}{2\pi}\sqrt{\frac{K_{ts}}{J_{Xeq}}} \tag{40}$$

$$J_{Xeq} = J_{mx} + 4(J_{bx})_{eq} \tag{41}$$

$$(J_{bx})_{eq} = m_{eq,t} \cdot r_t^2 \tag{42}$$

$$m_{eq,t} = c_{m,t} \cdot m_b \tag{43}$$

where J_{mx} is the rotational moment of inertia of the seismic mass, $(J_{bx})_{eq}$ is the effective rotational moment of inertia of the supported beams about the X-axis, $m_{eq,t}$ is the effective mass of the supported beam in the torsional vibration, and $r_t=(w_m\text{-}w_b)/2$ is the rotational radius about center C for the torsional vibration mode. The effective mass constant (Thomson and Dahleh 1998) of the supported beams for the torsional vibration mode, $c_{m,t}$ is approximately the same as the symmetric mode ($c_{m,s}$ = 13/35) because the kinetic energy due to the torsion is negligible compared with that due to the bending of the supported beams when the thin beam theory is assumed.

Following a similar integration like (24), the generated charge of a single beam is as follows:

$$Q_{t,b} = \frac{9\beta w_b d_{31} E_P (w_m - w_b)}{10 l_b} \cdot \left(\frac{t_P}{2} + a\right) \tag{44}$$

where β is the rotation angle of the seismic mass for the torsional vibration mode as follows:

$$\beta = \frac{m_{total,t} a_y Z_{c,t} l_b^3}{12(EI_Y)_{eq} w_m (w_m - w_b)} \tag{45}$$

$$m_{total,t} = m + 4 \cdot m_{eq,t} \tag{46}$$

where Zc,t is the distance between the equivalent system mass center for the torsional vibration mode and the neural axis.

Because of the design symmetry, the voltages collected from each beam, $V(a_i\text{-}b_i)$, for the torsional vibration mode will be of the same magnitude but different phases. The sensor's open-circuit voltage sensitivity S_y using the interconnection of the transducers as shown in Table 1 is as follows:

$$S_y = \frac{V_y}{a_y} = \frac{4Q_{t,b}}{a_y C_t} = \frac{12\beta d_{31} E_p t_p (w_m - w_b)}{l_b^2 \varepsilon_{33} a_y}\left(\frac{t_p}{2} + a\right) \tag{47}$$

Table 2 Dimensions of the triaxial accelerometer (μm)

l_b	1500
w_b	350
t_b	30
l_m	1300
w_m	4200
h_m	490
t_p	1

Table 3 Material parameters used for numerical evaluation of the analytical model

	Silicon	PZT
Piezoelectric coefficient matrix	N/A	*d*-matrix (50)
Density (kg/m^2)	2330	7550
Dielectric permittivity ε_{33}		6.46×10^{-9} (Hellwege and Hellwege 1981)
Young's modulus (N/m^2)	C_s-matrix (49)	C_p-matrix (48)

4. Verification using FEA

To verify the accuracy of the analytical model, finite element analysis using ANSYS is applied to compare the results. The dimensions of the exemplar device used in the following analysis are shown in Table 2. The material properties are listed in Table 3. The stiffness coefficient matrix of PZT is as (48). For the accelerometer fabricated using anisotropic wet etching as shown in Fig. 2, the transformed stiffness matrix (Wortman and Evans 1965) of silicon supported beams corresponding to the device coordinate system is as (49). The piezoelectric properties of PZT film have not yet been well determined, and hence the values of the bulk PZT 52/48 (Hellwege and Hellwege 1981) are used as shown in (50).

$$[C_p]=\begin{bmatrix} 11.425 & 5.8294 & 5.8525 & 0 & 0 & 0 \\ 5.8294 & 11.425 & 5.8525 & 0 & 0 & 0 \\ 5.8525 & 5.8525 & 9.8181 & 0 & 0 & 0 \\ 0 & 0 & 0 & 2.0747 & 0 & 0 \\ 0 & 0 & 0 & 0 & 2.0747 & 0 \\ 0 & 0 & 0 & 0 & 0 & 2.6042 \end{bmatrix} \times 10^{10}(N/m^2) \tag{48}$$

$$[C_S]=\begin{bmatrix} 19.44 & 3.52 & 6.39 & 0 & 0 & 0 \\ 3.52 & 19.44 & 6.39 & 0 & 0 & 0 \\ 6.39 & 6.39 & 16.57 & 0 & 0 & 0 \\ 0 & 0 & 0 & 7.96 & 0 & 0 \\ 0 & 0 & 0 & 0 & 7.96 & 0 \\ 0 & 0 & 0 & 0 & 0 & 5.09 \end{bmatrix} \times 10^{10}(N/m^2) \tag{49}$$

Table 4 Comparisons of the sensor responses with individual axial and triaxial accelerations (mV)

	$1\,\ddot{\ddot{x}}$	$1\,\ddot{\ddot{y}}$	$1\,\ddot{\ddot{z}}$	$1\ddot{\ddot{x}}+1\ddot{\ddot{y}}+1\ddot{\ddot{z}}$
Asymmetric	0.57	0	0	0.57
Torsional	0	0.43	0	0.43
Symmetric	0	0	4.38	4.38

Table 5 Comparisons of the resonant frequency (PZT film = 1μm) (Hz)

	Model	FEA	Error (%)
Symmetric	3270	3236	1.1
Asymmetric	12180	11717	4.0
Torsional	5474	5466	0.1

Table 6 Comparisons of the accelerometer sensitivity (PZT film = 1μm) (Unit: mV/g)

	Model	FEA	Error (%)
Symmetric	4.344	4.375	0.7
Asymmetric	0.569	0.572	0.5
Torsional	0.416	0.427	2.6

$$[d]=\begin{bmatrix} 0 & 0 & -93.5 \\ 0 & 0 & -93.5 \\ 0 & 0 & 223 \\ 0 & 494 & 0 \\ 494 & 0 & 0 \\ 0 & 0 & 0 \end{bmatrix} \times 10^{-12}(C/N) \tag{50}$$

To confirm the power of the configuration design of the accelerometer and the interconnection design of the transducers to eliminate the cross axis sensitivity, four different loads are applied including unit acceleration at three principal directions and a triaxial acceleration. The FEA results are shown in Table 4. When a triaxial acceleration is applied to the sensor; the sensor can identify the components of the accelerations using the interconnection design shown in Table 1. The responses are the same as individual axial component of acceleration applied to the accelerometer.

The comparisons between the analytical and the FEM results of the resonant frequencies and sensor sensitivities are presented in Table 5 and Table 6. In this case, the thickness of the PZT film is 1 (μm) that is relatively thin compared with the silicon beam of 30 (μm). The predictions agree very well with the FEM results with the errors for the resonant frequencies within 4% and the errors for the accelerometer sensitivities within 2.6 %. As the thickness of PZT varies from 0.5 to

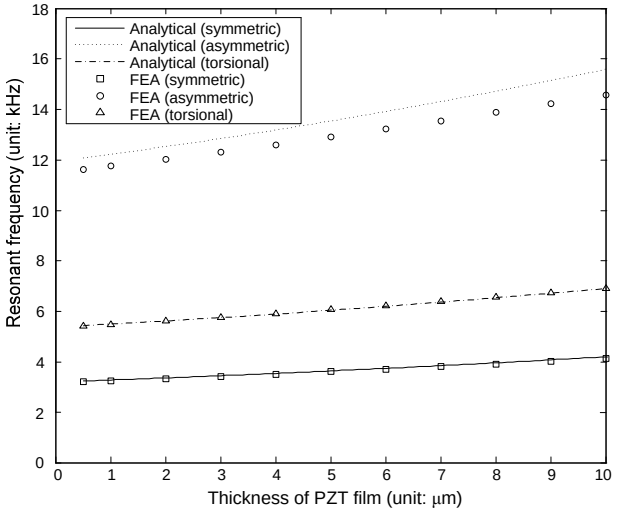

Fig. 11 Accelerometer resonant frequency vs. thickness of PZT film (Silicon beam l_b =1500 μm, w_b =350 μm, t_b =30 μm)

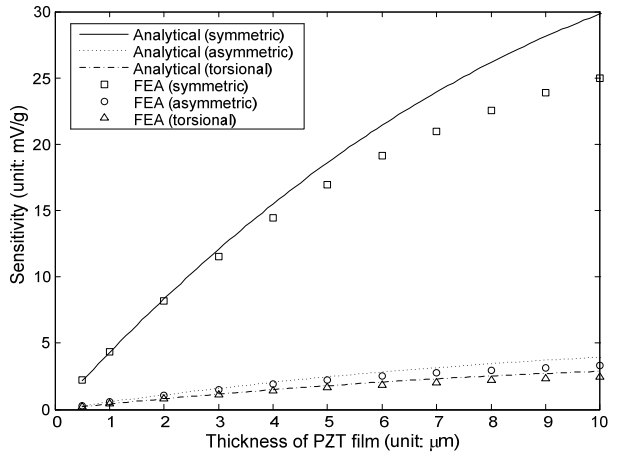

Fig. 12 Accelerometer sensitivities vs. thickness of PZT film (Silicon beam l_b =1500 μm, w_b =350 μm, t_b =30 μm)

10 (μm), the maximum prediction error for the resonant frequencies is still less than 5% as shown in Fig. 11. The predicted sensitivities of the accelerometers are still in good agreement with the FEA results for piezoelectric thin film. However, the prediction errors increase from 2.6% to 11% as the thickness of PZT increases from 0.5 to 10 (μm) as shown in Fig. 12. During the derivation of the analytical model, the supported beams are assumed under plane stress condition, and smaller strains and stresses are neglected as shown in (1) for simplification to derive the effective moduli of elasticity for silicon and the piezoelectric film. However, as one examines the strain distribution on the top surface of the laminated supported beam as shown in Fig. 13, the assumption, strain $\varepsilon_2 = 0$, is jeopardized when the thickness of PZT film increases, which might explain why the error of the predicted sensitivity increases as the thickness of PZT increases. Also, for simplicity, the estimation of the

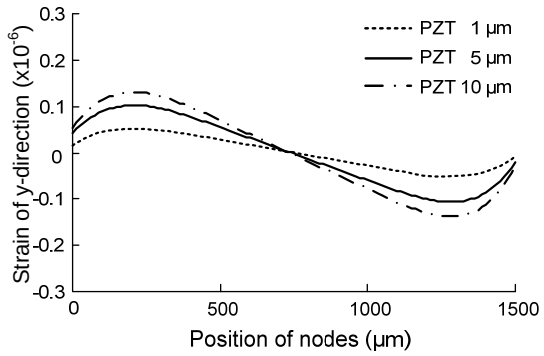

Fig. 13 Strain distributions on the top surface of the laminated supported beam with various thickness of PZT

generated charge of the piezoelectric transducer considers only the *X*-axial stress and the transverse piezoelectric charge to stress ratio d_{31} is a possible reason for the prediction error. However, the analytical model provides a good insight into the system variables that can be readily applied to the structure optimization and the design of the piezoelectric microaccelerometer.

5. Conclusion

This study proposed the design and the system modeling of a triaxial piezoelectric micro-accelerometer and presented the analytical models of the resonant frequency and the sensitivities for triaxial accelerations. The model applies laminated beam theory to include the mechanical stiffness of the piezoelectric layer. The effective mass of the supported beams for three vibration modes: symmetric, asymmetric and torsional are considered in the modeling of the resonant frequency and sensor sensitivities using energy method. Therefore, the model applies to the accelerometer with a thick piezoelectric film. A special interconnection design of the piezoelectric transducers eliminates cross axis sensitivity, and provides accurate measurement of triaxial accelerations using the simple configuration. The triaxial sensitivities may differ by an order for the current design, which can be minimized by proper parameter design. The analytical results of the resonant frequency and sensor sensitivities are in good agreement with the FEA results. Although the prediction errors of the sensor sensitivities slightly increase with the increase of PZT thickness, the analytical models provide a good insight into the characterization of the triaxial microaccelerometer that can be applied to future design optimization.

Acknowledgments The authors would like to thank the National Science Council of the Republic of China, Taiwan, for financially supporting this research under Contract No. NSC 97-2221-E-327 -011 -MY2.

References

Chae J., Kulah H., Najafi K. (2005) A monolithic three-axis micro-g micromachined silicon capacitive accelerometer. *J. Microelectromech. System* 14, 2: 235–241.

DeVoe D. L., Pisano A. P. (2001) Surface micromachined piezoelectric accelerometers. *J. Microelectromech. System* 10, 2: 180-186.

Gere J. M., Timoshenko S. P. (1997) *Mechanics of Materials*, 4th ed., PWS Publishing Company, Boston, MA.

Hellwege K.-H., Hellwege A.M. (eds.) (1981) *Ferroelectrics and related substances,* Springer-Verlag Berlin, Heidelberg, New York: 123.

Hindrichsen C.C., Almind N.S., Brodersen S.H., Hansen O., Thomsen E.V. (2009) Analytial model of a PZT thick-film triaxial acceleromter for optimum design. *IEEE Sensor Journal* 9, 4: 419-429.

Kunz K., Enoksson P., Stemme G. (2001) Highly sensitive triaxial silicon accelerometer with integrated PZT thin film detectors. *Sensors and Actuators* A 92, 1: 156-160.

Lemkin M. A., Boser B. E., Auslander D., Smith J. H. (1997) A 3-axis balanced accelerometer using a single proof-mass. *Proc. Transducer*, Chicago, IL, Jun. 16–19: 1185–1188.

Lowrie C., Desmulliez M.P.Y., Hoff L., Elle O.J., Fosse E. (2009) MEMS three-axis accelerometer: Design, fabrication and application of measuring heart wall motion. *Proceedings of Design, Test, Integration & Packaging of MEMS/MOEMS*: 229-234.

Takao H., Fukumoto H., Ishida M. (2001) A CMOS integrated three-axis accelerometer fabricated with commercial submicrometer CMOS technology and bulk-micromachining. *IEEE Trans. Electron Devices*; 48, 9:. 1961–1968.

Thomson W. T., Dahleh M. D. (1998) *Theory of vibration with application*, 5th ed. Prentice-Hall, New Jersey: 23.

Timoshenko S.P., Goodier J. N. (1970) *Theory of Elasticity*, 3rd ed. McGraw-Hill, New York: 109.

van Kampen R.P., Wolffenbuttel R.F. (1998) Modeling the mechanical behavior of bulk-micromachined silicon accelerometers. *Sensors and actuators* A 64: 137-150.

Wang L.-P., Wolf R.A., Jr., Wang Y., Deng K.K., Zou L., Davis R.J., Trolier-McKinstry S. (2003) Design fabrication and measurement of high-sensitivity piezoelectric microelectromechanical systems accelerometers. *Journal of Microelectromechanical Systems* 12, 4: 433 - 439.

Wang Q.-M., Yang Z., Li F., Smolinski P. (2004) Analysis of thin film piezoelectric microaccelerometer using analytical and finite element modeling. *Sensors and Actuators* A 113, 1: 1-11.

Wortman J. J. and Evans R. A. (1965) Young's modulus, shear modulus, and Poisson's ratio in silicon and germanium. *Journal of applied physics* 36, 1: 153-156.

Yu J.-C., Lan C.-B. (2001) System modeling of microaccelerometer using piezoelectric thin films. *Sensors and Actuators* A 88, 2: 178-186.

Zhu M., Kirby P., Lim M.Y. (2004) Lagrange's formalism for modeling of a triaxial microaccelerometer with piezoelectric thin-film sensing. *IEEE Sensors Journal* 4, 4: 455-463.

Zou Q.; Tan W.; Kim E. S.; Loeb G.E. (2008) Single- and Triaxis Piezoelectric-Bimorph Accelerometers. *Journal Of Microelectromechanical Systems* 17, 1: 45-57.